INTERNATIONAL JOURNAL FOR NUMERICAL METHODS IN FLUIDS
Int. J. Numer. Meth. Fluids 2008; **58**:183–212
Published online 18 February 2008 in Wiley InterScience (www.interscience.wiley.com). DOI: 10.1002/fld.1722

A conservative unstructured scheme for rapidly varied flows

Stephan C. Kramer[1, 2, *, †] and Guus S. Stelling[1]

[1]*Environmental Fluid Mechanics Section, Faculty of Civil Engineering and Geosciences, Delft University of Technology, Stevinweg 1, 2628 CN Delft, The Netherlands*
[2]*Applied Modelling and Computation Group (AMCG), Department of Earth Science and Engineering, South Kensington Campus, Imperial College London, London SW7 2AZ, U.K.*

SUMMARY

This article introduces a new semi-implicit, staggered finite volume scheme on unstructured meshes for the modelling of rapidly varied shallow water flows. Rapidly varied flows occur in the inundation of dry land during flooding situations. They typically involve bores and hydraulic jumps after obstacles such as road banks. Near such sudden flow transitions, the grid resolution is often low compared with the gradients of the bathymetry. Locally the hydrostatic pressure assumption may become invalid. In these situations, it is crucial to apply the correct conservation properties to obtain accurate results. An important feature of this scheme is therefore its ability to conserve momentum locally or, by choice, preserve constant energy head along a streamline. This is achieved using a special interpolation method and control volumes for momentum.

The efficiency of inundation calculations with locally very high velocities, and in the case of unstructured meshes locally very small grid distances, is severely hampered by the Courant condition. This article provides a solution in the form of a locally implicit time integration for the advective terms that allows for an explicit calculation in most of the domain, while maintaining unconditional stability by implicit calculations only where necessary.

The complex geometry of flooded urban areas asks for the flexibility of unstructured meshes. The efficient calculation of the pressure gradient in this, and other semi-implicit staggered schemes, requires, however, an orthogonality condition to be put on the grid. In this article a simple method is introduced to generate unstructured hybrid meshes that fulfil this requirement. Copyright © 2008 John Wiley & Sons, Ltd.

Received 24 April 2007; Revised 5 November 2007; Accepted 9 November 2007

KEY WORDS: rapidly varied flow; inundation; unstructured mesh; hybrid mesh; conservation properties; momentum conservation; advection; locally implicit; flooding and drying

*Correspondence to: Stephan C. Kramer, Applied Modelling and Computation Group (AMCG), Department of ESE, South Kensington Campus, Imperial College London, London SW7 2AZ, U.K.
†E-mail: stephan.kramer@imperial.ac.uk

1. INTRODUCTION

The numerical modelling of rapidly varied shallow water flows typically found in flooding situations after, for example, dike breaks or tsunamis is a complex and computationally demanding task. To enable the simulation of flooding in a large urban area, including all the details at the street level, a very efficient scheme is needed. The complex geometry asks for the flexibility of unstructured grids. In this paper we will show how the techniques of the staggered Cartesian conservative scheme of [1] can be extended for the application to unstructured grids. This scheme is able to deal accurately with large gradients in the flow near steep bottom gradients and in hydraulic jumps and bores. Here the conservation properties of the scheme are important to obtain physically realistic solutions. In case of relatively steep gradients caused by a lack of grid resolution, a much faster convergence can be achieved if the right conservation properties are observed.

Many shallow water models for large-scale simulations are based on the application of staggered grids. They provide efficiency and accuracy for sub-critical hydrostatic flows, in particular, in combination with A.D.I. [2, 3] or semi-implicit [4, 5] time integration. Their unconditional stability allows deep water to be simulated next to shallow water without severe time step restrictions, unlike explicit shallow water equation schemes where the stability is dependent on the wave celerity and therefore on the depth. In [6] it is shown how semi-implicit unstructured staggered schemes can maintain their unconditional stability in the presence of the Coriolis force. The scheme of Casulli [4] combines a semi-implicit time integration of the equations with a semi-Lagrangian approach for the advection term. Such an approach, however, is unable to provide the desired momentum conservation. In [1] it is shown how conservation can be achieved by combining the semi-implicit scheme with an advection scheme with a special choice for the discretization of the advective velocity based on the local momentum balance.

Many shock-capturing methods, especially for unstructured grids, are based on approximate Riemann solvers or Godunov-type methods on collocated grids [7, 8]. In general, they lack the efficiency of semi-implicit methods on staggered grids. A locally conservative scheme for unstructured staggered grids is given by Perot [9]. For local momentum conservation of a scheme, a local balance of the full momentum vector must be derived. The full momentum vector is not directly available in staggered schemes, only face normal velocities are stored, and in the case of unstructured meshes it is also not possible to treat the velocity components independently. This poses a general difficulty in deriving unstructured staggered schemes that conserve momentum locally. In [9] this is done by showing equivalence to a cell-based balance using a special velocity interpolation. Another unstructured staggered method is given in [10] in the context of the so-called Mach-uniform methods. Although not provably conservative, its results appear to give the desired conservation and shock-capturing properties. In this paper it will be shown how the advection scheme of both methods can be combined with a semi-implicit time integration.

The semi-implicitly discretized equations can be solved in an efficient way for both structured and unstructured grids, as long as they are orthogonal. *Unstructured orthogonal grids* are unstructured grids in which each line segment connecting the cell centres of two adjacent cells has a non-empty and orthogonal intersection with the shared face of the two cells [11]. Triangular grids with only acute triangles satisfy this condition, but the generation of such grids is far from trivial [12]. For this reason, this paper presents an alternative method for generating orthogonal grids with the same flexibility to accurately represent the boundaries of the flow domain.

In Section 2 we first briefly review how the shallow water equations are solved following Casulli's method. In Section 3 we discuss the conservation properties that play a role in the modelling

DOI: 10.1002/fld

of rapidly varied flows. Section 4 presents two discretizations of the depth-integrated momentum equation based on [9, 10]. Further, it will be shown how they can be combined with the non-conservative formulation used in Casulli's scheme. In Section 5 we demonstrate how the advection scheme can be made unconditionally stable by applying a locally implicit time integration scheme. In Section 6 we present a modified cut-cell technique that produces grids that are unstructured along the boundaries and Cartesian in the interior. It satisfies the orthogonality condition of the numerical scheme and combines the advantages of Cartesian grids with the flexibility of unstructured grids. In Section 7 some test cases are given that demonstrate both the shock-capturing capabilities of the numerical scheme and the efficacy of the hybrid grid technique.

2. SEMI-IMPLICIT METHOD FOR THE SHALLOW WATER EQUATIONS

This section briefly outlines the semi-implicit discretization of the shallow water equations as in [4] on two-dimensional unstructured meshes (see also [11]). The two-dimensional shallow water equations in non-conservative form are given by

$$\frac{\partial h}{\partial t}+\frac{\partial (uh)}{\partial x}+\frac{\partial (vh)}{\partial y}=0 \tag{1a}$$

$$\begin{aligned}\frac{\partial u}{\partial t}+u\frac{\partial u}{\partial x}+v\frac{\partial u}{\partial y}+g\frac{\partial \zeta}{\partial x}+c_f\frac{u\|u\|}{h}&=0\\ \frac{\partial v}{\partial t}+u\frac{\partial v}{\partial x}+v\frac{\partial v}{\partial y}+g\frac{\partial \zeta}{\partial y}+c_f\frac{v\|u\|}{h}&=0\end{aligned} \tag{1b}$$

where ζ is the water level above a plane of reference, h the total water depth, u and v are the depth-averaged velocities in, respectively, x- and y-directions and c_f is the dimensionless bottom friction coefficient. Furthermore, we define a downward measured bottom level b, so that $h=\zeta+b$.

We consider a two-dimensional unstructured grid consisting of cells that are arbitrary polygons. The flow variables are stored in a staggered setting to avoid spurious pressure modes. The water levels are stored in the cell centres and the normal component of the velocity in the middle of each cell face. For a fixed bottom topography, we may replace the time derivative of the water depth h in the mass continuity equation (1a) with that of the water level ζ. A finite volume discretization in cell c then reads

$$A_c\frac{\mathrm{d}\zeta_c}{\mathrm{d}t}+\sum_{k\in S_c}\pm_c^f l_f\,{}^*h_f u_f=0 \tag{2}$$

where A_c is the cell area, and S_c is the set of sides of cell c. For each $k\in S_c$, l_f denotes the length of the side, and u_f the face normal component of the velocity. $\pm_c^f$ is $+1$ if the face normal is pointing outward of cell c and -1 if pointing inward. The water height ${}^*h_f$ at the face is defined as

$${}^*h_f=\begin{cases}\min(b_{c_\mathrm{L}},b_{c_\mathrm{R}})+h_{c_\mathrm{L}} & \text{for } u_f>0\\ \min(b_{c_\mathrm{L}},b_{c_\mathrm{R}})+h_{c_\mathrm{R}} & \text{for } u_f>0\end{cases} \tag{3}$$

DOI: 10.1002/fld

Thus, the water height used in the outward fluxes of a cell is at most that of the cell itself. This choice guarantees a positive water height in a cell c if for all its faces f with outward going flux we have

$$\Delta t l_f |u_f| < A_c \tag{4}$$

This condition is independent of the water height itself, thus avoiding very strict time step restrictions for very shallow water layers.

The momentum equation (1b) at face f is discretized by

$$\frac{\mathrm{d}u_f}{\mathrm{d}t} + g\frac{\zeta_{c_\mathrm{R}} - \zeta_{c_\mathrm{L}}}{\Delta x_f} + \mathrm{Adv}(u_f) + c_f \frac{u_f \|u_f\|}{\bar{h}_f} = 0 \tag{5}$$

$\mathrm{Adv}(u_f)$ is the discretization of the advection terms in (1b) that are described in the following two sections. Δx_f is the length of the line segment between the centres of the cells c_L and c_R that lies on either side of f. In an orthogonal grid, this line segment is by definition orthogonal to the cell face and thus in the direction of the face normal. This allows for a simple calculation of the hydrostatic pressure gradient out of the water levels in the two adjacent cell centres only (Figure 1). The transversal component of the velocity vector in f, needed for the computation of $\|u_f\|$, follows from the velocity reconstruction of the advection discretization described below.

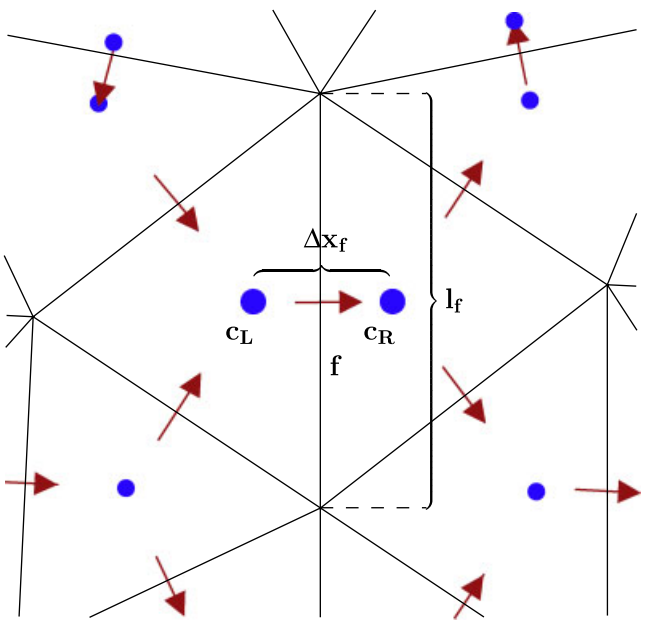

Figure 1. The geometric quantities are l_f length of a face f, and Δx_f distance between its adjacent cell centres, used in Equations (2) and (5). The orientation of the face normal at face f is such that it is pointing out of cell c_L and into c_R; hence, we use $\pm^f_{c_\mathrm{L}} = 1$ and $\pm^f_{c_\mathrm{R}} = -1$.

DOI: 10.1002/fld

After time integration of (5) by the θ-method, we obtain

$$\frac{u_f^{n+1}-u_f^n}{\Delta t}+g\frac{\zeta_{c_\mathrm{R}}^{n+\theta}-\zeta_{c_\mathrm{L}}^{n+\theta}}{\Delta x_f}+\mathrm{Adv}(u_f^{n+*})+c_f\frac{\|u_f^n\|u_f^{n+1}}{\bar{h}_f}=0 \qquad (6)$$

$$\zeta^{n+\theta}=(1-\theta)\zeta^n+\theta\zeta^{n+1}$$

Given the velocities and water heights at the old time level, this equation relates the new velocity u_f^{n+1} to the new water heights $\zeta_{c_\mathrm{L}}^{n+1}$ and $\zeta_{c_\mathrm{R}}^{n+1}$ at time t^{n+1}. Following [4] we substitute this expression for u_f^{n+1} in the time-integrated version of (2),

$$A_c\frac{\zeta_c^{n+1}-\zeta_c^n}{\Delta t}+\sum_{k\in S_c}\pm_c^f l_f{}^*h_f^n u_f^{n+\theta}=0 \qquad (7)$$

The resulting equation relates the new water height ζ_c^{n+1} in a cell c to the new water heights of its adjacent cells. The complete linear system of equations with water heights as unknowns is symmetric and positive definite and can therefore be solved efficiently by means of, e.g. the conjugate gradient method. Finally, the new velocities are computed substituting the new water heights in (6).

The semi-implicit time integration makes the stability of the scheme independent of the celerity [4]. An explicit treatment of the advection term $\mathrm{Adv}(u_f)$, however, still imposes a Courant condition, restricting the time step in the presence of large velocities or small cells anywhere in the domain. An unconditionally stable scheme can be derived with a semi-Lagrangian approach as in [4]. A disadvantage of such schemes is that they do not provide the desired conservation of momentum. A conservative advection scheme will be derived in the following two sections. In Section 5 it will be shown how this scheme can be made unconditionally stable.

3. CONSERVATION PRINCIPLES IN RAPIDLY VARIED FLOWS

The two-dimensional shallow water equations are derived from the incompressible Navier–Stokes equations using the hydrostatic pressure assumption. At local discontinuities, this assumption may no longer be valid. Here the equations also no longer have a unique solution. An accurate computation would require a three-dimensional non-hydrostatic model. However, the applications of proper conservation laws based on physical considerations are often sufficient to derive large-scale properties, such as shock speeds and energy losses. The conservation laws that play a role are the mass balance (1a), which should always be maintained, and conservation of momentum and energy head.

3.1. Conservation of momentum

From the hydrostatic pressure assumption

$$\frac{\partial p}{\partial z}=\rho g \qquad (8)$$

(and constant density) it follows that the horizontal pressure gradient is constant over the vertical. The pressure gradient term in the depth-integrated momentum balance can therefore be expressed

DOI: 10.1002/fld

as h times the gradient of the water surface:

$$\frac{\partial \mathbf{q}}{\partial t} + \nabla \cdot (\mathbf{qu}) + gh\nabla\zeta = 0 \tag{9}$$

For a non-continuous water surface, however, this expression is not well defined, since the weak solution depends on the value of h at the discontinuity. Here the following jump conditions have to be applied

$$s\Delta h = \Delta q_n \tag{10a}$$

$$s\Delta q_n = \Delta F, \quad F = \tfrac{1}{2} gh^2 + q_n u_n \tag{10b}$$

where s is the shock speed, and q_n and u_n are the vectors $\mathbf{q}$ and $\mathbf{u}$ projected in the direction normal to the shock, respectively. They enforce conservation of mass and momentum, respectively, across the jump. The pressure term in the momentum balance can be derived again integrating the pressure gradient over the vertical. Here it is important, however, to take in account the pressure gradient over the vertical interface at the front of the bore.

To ensure satisfaction of the momentum jump condition (10b) many numerical schemes are based on the following momentum equation:

$$\frac{\partial \mathbf{q}}{\partial t} + \nabla \cdot (\mathbf{qu}) + \frac{1}{2} g\nabla h^2 = -gh\nabla b \tag{11}$$

in which the pressure gradient term is split into a flux term and a 'bottom slope force' as a source term. Numerical solutions of a finite volume discretization of this equation converge to a weak solution that automatically satisfies the jump condition. The splitting of the pressure gradient term, however, creates its own problems as the two terms do not represent independent physical phenomena. If for instance one applies a higher-order interpolation for the flux $\frac{1}{2} gh^2$ at the boundary of a control volume, it no longer matches the bottom slope term. This easily leads to artificial flow near a bottom gradient in water initially at rest [13]. Moreover, the bottom slope term in (11) still has an ambiguity for the value of h at discontinuities in the bottom topography.

To arrive at physically realistic solutions in rapidly varied flows with steep bottom gradients, it is important that the jump condition (10b) is applied only as an algebraic equation at the shock itself and that the differential equation (9) is applied to the rest of the domain. In the following a discretization it is called momentum conservative if it is consistent with (9) and satisfies the jump condition (10b) across a discontinuity in the water surface.

3.2. Constancy of energy head

Bernoulli's equation gives that along a streamline in a steady flow

$$\frac{\partial}{\partial \sigma}\left(\rho g z + p + \frac{1}{2}\rho u^2\right) = 0 \tag{12}$$

Assuming hydrostatic pressure, it follows that the energy head

$$H = \zeta + \frac{u^2}{2} g \tag{13}$$

is constant along a streamline in a steady shallow water flow.

DOI: 10.1002/fld

The basic principles of conservation of momentum and energy head are used in channel hydraulics to calculate the flow, especially near sudden expansions or contractions. In a sudden channel expansion, for instance the flow after a weir, the application of momentum conservation leads to a loss of energy head. This conforms with the fact that energy is dissipated in turbulent flow right after the expansion. Hence, by applying momentum conservation and comparing the energy head upstream and downstream of the transition, one can calculate the energy head loss.

On the other hand, momentum conservation based on (8) in sudden channel contractions would lead to an increase of energy, which is an unrealistic assumption from a physical point of view. In the flow over a sudden rise in the bottom level, the streamlines are almost vertical; hence, the hydrostatic pressure assumption is no longer valid. Unknown forces on the bottom obstacle have to be taken into account. As long as these forces are normal to the flow direction, no work is done upon the flow, and the energy balance is still valid. Hence, in this case it is better to apply the energy head balance. The same should be done for flow contractions, in general, perhaps with some additional head losses, to avoid unrealistic energy increases.

It is to be noted that smooth solutions of the shallow water equations in non-conservative form (1) always satisfy both momentum conservation as in (9) and constancy of energy head along streamlines. For sudden changes in bathymetry or water level, however, it is better to go back to the elementary principles of the physical balances from open channel hydraulics. If the changes are sudden relative to the grid size; hence, due to a lack of grid resolution, a numerical scheme that adheres to these principles will converge faster to a physically realistic solution than a scheme that is merely consistent with (1).

4. CONSERVATIVE DISCRETIZATION OF THE MOMENTUM BALANCE

In this section a discretization of the momentum equation (9) is derived that satisfies the conservation requirements from the previous section. In a velocity point of the staggered grid only the face normal component is considered. Thus, momentum equation (9) reduces to

$$\frac{\partial \mathbf{q}\cdot\mathbf{n}}{\partial t}+\boldsymbol{\nabla}\cdot(\mathbf{q}\mathbf{u}\cdot\mathbf{n})+gh\mathbf{n}\cdot\boldsymbol{\nabla}\zeta=0 \tag{14}$$

This balance is applied to a control area constructed out of the two adjacent cells next to the velocity point. The scheme in [1] uses exactly half of both cells, namely the square in between the two cell centres. This gives us a complete cover of adjacent control areas for the momentum in both the x- and y-directions (see Figure 2). If the numerical fluxes at the boundary between adjacent control areas match, the momentum balance in an arbitrary number of adjacent control areas can be combined such that all internal fluxes cancel. Thus, a local balance is created for the combined area. This is a necessary condition to prove convergence to a conservative solution by the Lax–Wendroff theorem [14].

In unstructured staggered grids, things are more complicated. As the velocity components at the cell faces are in arbitrary direction, the local balances around the velocity points are not independent. In order to show that a method is locally conservative, one should be able to reconstruct a balance of the full momentum vector out of the velocity components in an arbitrary region of the grid. For the scheme of Perot [9], this is accomplished by reconstructing cell-based momentum vectors out

DOI: 10.1002/fld

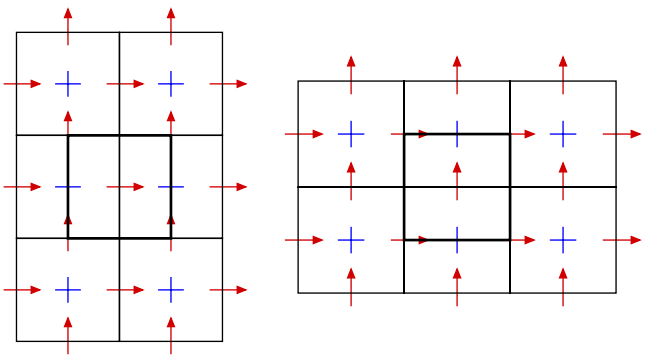

Figure 2. Control volumes for the momentum in the x-direction (left figure) and the y-direction (right figure) of the Cartesian scheme.

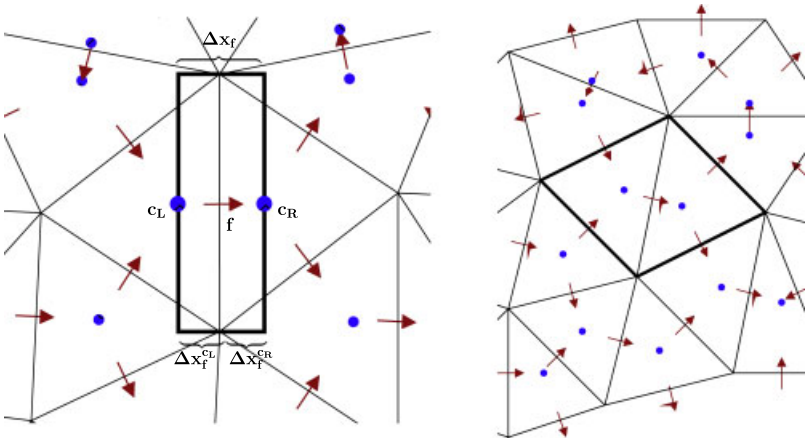

Figure 3. Control volumes for the momentum at a face in Perot's scheme (left figure) and Wenneker's scheme (right figure).

of the face normal components, so that a local balance can be made by adding the balances for each cell.

4.1. Cell-centred and face-centred control volumes

The scheme of Perot [9] in fact employs a transformation between face-centred control volumes and cells. The face-centred control area consists of the rectangle in between the circumcentres of the two adjacent triangles, similar to the Cartesian case (see the left picture in Figure 3). The width and height of this rectangle are given by the length of the face and the distance between the circumcentres. This distance is expressed as the sum of the distance between the left triangle centre and the face, and the distance between the face and the right triangle centre:

$$\Delta x_f = \Delta x_f^{c_L} + \Delta x_f^{c_R} \tag{15}$$

DOI: 10.1002/fld

A cell-based momentum vector $\mathbf{q}_c$ is interpolated out of the normal components q_f stored at the cell faces by

$$A_c\mathbf{q}_c = \sum_{\substack{f \\ \text{cell} \\ \text{faces}}} l_f \Delta x_f^c q_f \mathbf{n}_f \tag{16}$$

where A_c is the area of the cell and $\mathbf{n}_f$ are the normal vectors at the faces. The reconstruction of the full momentum vector is a first-order interpolation for any polygon-shaped cell with a common circumcentre. This follows from the following geometrical identity:

$$\sum_{\substack{f \\ \text{cell} \\ \text{faces}}} l_f \Delta x_f^c \mathbf{n}_f \mathbf{n}_f^T = A_c \mathbf{I} \tag{17}$$

where $\mathbf{n}_f\mathbf{n}_f^{\mathrm{T}}$ are 2×2 matrices that result from multiplying the normal vectors with their transposed, and $\mathbf{I}$ is the $\mathbb{R}^2$ identity matrix. If we make the first-order assumption that the vector field $\mathbf{q}$ is constant in a cell and fill in $q_f = \mathbf{q}\cdot\mathbf{n}_f = \mathbf{n}_f^{\mathrm{T}}\mathbf{q}_f$ at the cell faces, this identity guarantees that the interpolated cell vector returns the original vector $\mathbf{q}$. The common circumcentre requirement makes that we can use any triangle and only a restricted class of quadrilaterals, and rectangles among others.

A local balance can now be reconstructed by adding all $A_c\mathbf{q}_c$ terms of all cells in the balance area. By combining the contribution of a face to its left and right cells, we can rewrite this into a sum of contributions of all faces in the area:

$$\sum_{\substack{c \\ \text{cells}}} A_c\mathbf{q}_c = \sum_{\substack{f \\ \text{faces}}} l_f \Delta x_f^{c_{\mathrm{L}}} q_f \mathbf{n}_f + l_f \Delta x_f^{c_{\mathrm{R}}} q_f \mathbf{n}_f = \sum_{\substack{f \\ \text{faces}}} l_f \Delta x_f q_f \mathbf{n}_f \tag{18}$$

where for faces at the boundary of the area there is only a contribution to one side of the face, so we consider the other $\Delta x_f^c = 0$. In this way we can indeed see the balance as a sum of contributions from control areas around the velocity points with area $\Delta x_f l_f$.

The other way around it is also possible to reconstruct face normal components a_f out of a given set cell-based vectors $\mathbf{a}_c$, by taking the following linear combination of the two adjacent cell vectors at each face

$$a_f = \frac{\Delta x_f^{c_{\mathrm{L}}}}{\Delta x_f}\ \mathbf{a}_{c_{\mathrm{L}}}\cdot\mathbf{n}_f + \frac{\Delta x_f^{c_{\mathrm{R}}}}{\Delta x_f}\ \mathbf{a}_{c_{\mathrm{R}}}\cdot\mathbf{n}_f \tag{19}$$

It is now easy to show that again the cell-centred balance corresponds with the momentum balance obtained by adding the face components, i.e.

$$\sum_{\substack{c \\ \text{cells}}} A_c\mathbf{a}_c = \sum_{\substack{f \\ \text{faces}}} l_f \Delta x_f\ a_f \mathbf{n}_f \tag{20}$$

4.2. Conservative scheme based on Perot's scheme

The duality between face-centred and cell-centred control volumes is used in Perot's scheme to derive a staggered scheme, for which the conservation properties can be expressed in cell-centred control volumes with full velocity vectors in the same way as for collocated schemes. First we

DOI: 10.1002/fld

write down a very general finite volume discretization $A_c\mathbf{a}_c$ of the advection term $\nabla\cdot\mathbf{qu}$ integrated over a cell in a conservative collocated scheme. Using Gauss' theorem, we obtain

$$\int_{\text{cell}} \nabla\cdot\mathbf{qu} = \sum_{\substack{f \\ \text{cell} \\ \text{faces}}} \int_{\text{face}\,f} \mathbf{q}\cdot\mathbf{n}_f\mathbf{u} \approx \sum_{\substack{f \\ \text{cell} \\ \text{faces}}} Q_f\mathbf{u}_f = A_c\mathbf{a}_c \tag{21}$$

where Q_f is $\mathbf{q}_f\cdot\mathbf{n}_f$ integrated along face f, i.e. the flux going through this face, and $\mathbf{u}_f$ is the velocity vector interpolated at face f.

Using (19) we obtain the corresponding expression for the advection integrated over the control area of each face. In this way, a staggered advection scheme can be derived with a local momentum balance that is equal to that of the collocated scheme:

$$\Delta x_f l_f \frac{\mathrm{d}q_f}{\mathrm{d}t} + l_f(\Delta x_f^{c_\mathrm{L}}\mathbf{a}_{c_\mathrm{L}} + \Delta x_f^{c_\mathrm{R}}\mathbf{a}_{c_\mathrm{R}})\cdot\mathbf{n}_f = 0 \tag{22}$$

For the discretization of the pressure gradient term, we define the following consistent depth at the face:

$$\tilde{h}_f = \frac{\zeta_{c_\mathrm{L}} + \zeta_{c_\mathrm{R}}}{2} + \frac{\Delta x_f^{c_\mathrm{L}}}{\Delta x} b_{c_\mathrm{L}} + \frac{\Delta x_f^{c_\mathrm{R}}}{\Delta x} b_{c_\mathrm{R}} \tag{23}$$

so that we obtain the following discretization of (14)

$$\frac{\mathrm{d}q_f}{\mathrm{d}t} + \left(\frac{\Delta x_f^{c_\mathrm{L}}}{\Delta x_f}\mathbf{a}_{c_\mathrm{L}} + \frac{\Delta x_f^{c_\mathrm{R}}}{\Delta x_f}\mathbf{a}_{c_\mathrm{R}}\right)\cdot\mathbf{n}_f + g\tilde{h}_f\frac{\zeta_{c_\mathrm{R}} - \zeta_{c_\mathrm{L}}}{\Delta x_f} = 0 \tag{24}$$

The specific choice of $\tilde{h}_f$ gives the most accurate representation of the water volume above the control area for discontinuities in the bed that are situated exactly at the cell boundaries. As long as the water surface is smooth, the scheme gives a consistent discretization of the water volume times a pressure gradient, thus avoiding artificial flow near sharp bottom gradients.

To study the convergence behaviour for discontinuous water surfaces, note that the definition of $\tilde{h}_f$ is independent of the chosen reference level. Therefore in a small region of size ε around a jump in the water level, we may assume $b = 0 + \mathcal{O}(\varepsilon)$ for a smooth bottom and express $\tilde{h}_f = \frac{1}{2}\zeta_{c_\mathrm{L}} + \frac{1}{2}\zeta_{c_\mathrm{R}} + \mathcal{O}(\varepsilon)$. However, also $\zeta_{c_\mathrm{L}} = h_{c_\mathrm{L}} + \mathcal{O}(\varepsilon)$ and $\zeta_{c_\mathrm{R}} = h_{c_\mathrm{R}} + \mathcal{O}(\varepsilon)$. This means that the pressure gradient term in this region can be approximated by

$$g\tilde{h}_f\frac{\zeta_{c_\mathrm{R}} - \zeta_{c_\mathrm{L}}}{\Delta x_f} \approx \frac{\frac{1}{2}gh_{c_\mathrm{R}}^2 - \frac{1}{2}gh_{c_\mathrm{L}}^2}{\Delta x_f} + \mathcal{O}(\varepsilon) \tag{25}$$

With this approximation of the pressure gradient (24) becomes completely identical to the scheme of Perot in [9] using a pressure $p = \frac{1}{2}gh^2$. From the conservation properties of this scheme, it follows that the solutions will converge to a weak solution with the right jump condition as in (10b). Because in the region our scheme is close to Perot's pressure gradient, for $\varepsilon \to 0$ also the solutions of our scheme will converge to the right jump condition. In the rest of the domain (with smooth water surface), the scheme will give the correct momentum conservative solutions (assuming a hydrostatic pressure) even for arbitrarily steep or discontinuous beds.

DOI: 10.1002/fld

4.3. Conservative scheme based on Wenneker's scheme

Another momentum advection scheme for unstructured staggered grids is given in [10]. Instead of the rectangle between the circumcentres, it considers the two entire triangles at either side of a face together as the control area for the face. This gives the following scheme:

$$\frac{\mathrm{d}q_f}{\mathrm{d}t}+\left(\sum_k^{\text{4 faces of the CA}} Q_k {}^*\mathbf{u}_k\right)\cdot\mathbf{n}_f+g\tilde{h}_f\frac{\zeta_{c_\mathrm{R}}-\zeta_{c_\mathrm{L}}}{\Delta x_f}=0 \tag{26}$$

where we sum over the four faces around the control area.

Compared with Perot's scheme it has a different weighting of the contribution to the advection term of the left and right cells. Introducing the following weighting factors

$$\alpha_f^{c_\mathrm{L}}=\frac{\Delta x_f^{c_\mathrm{L}}}{\Delta x_f},\quad \alpha_f^{c_\mathrm{R}}=\frac{\Delta x_f^{c_\mathrm{R}}}{\Delta x_f}\quad \text{for Perot's scheme} \tag{27}$$

and

$$\alpha_f^{c_\mathrm{L}}=\frac{A_{c_\mathrm{L}}}{A_{c_\mathrm{L}}+A_{c_\mathrm{R}}},\quad \alpha_f^{c_\mathrm{R}}=\frac{A_{c_\mathrm{R}}}{A_{c_\mathrm{L}}+A_{c_\mathrm{R}}}\quad \text{for Wenneker's scheme}$$

Both schemes can be expressed in the following general form:

$$\frac{\mathrm{d}q_f}{\mathrm{d}t}+\left(\alpha_f^{c_\mathrm{L}}\mathbf{a}_{c_\mathrm{L}}+\alpha_f^{c_\mathrm{R}}\mathbf{a}_{c_\mathrm{R}}\right)\cdot\mathbf{n}_f+g\tilde{h}_f\frac{\zeta_{c_\mathrm{R}}-\zeta_{c_\mathrm{L}}}{\Delta x_f}=0 \tag{28}$$

Note that for Wenneker's scheme the flux through face f itself going out of the upwind cell cancels against the flux going into the downwind cell. The pressure gradient discretization of [10] is different than ours, since in [10] centroids instead of circumcentres are used to store water levels. The water depth $\tilde{h}_f$ should be adjusted using the control area of Wenneker's scheme. We can again express it in a general form, which is valid for both schemes

$$\tilde{h}_f=\frac{\zeta_{c_\mathrm{L}}+\zeta_{c_\mathrm{R}}}{2}+\alpha_f^{c_\mathrm{L}}b_{c_\mathrm{L}}+\alpha_f^{c_\mathrm{R}}b_{c_\mathrm{R}} \tag{29}$$

For Wenneker's scheme, there is no proof that it is conservative, but in test cases it shows the right convergence behaviour towards conservative solutions [10].

4.4. Depth-integrated versus depth-averaged formulation

A problem with the schemes of (24) and (26) is that they are based on depth-integrated velocities $\mathbf{q}$, whereas the semi-implicit scheme from Section 2 that we wish to employ uses depth-averaged velocities $\mathbf{u}$. We show, however, that both schemes can be rewritten in u-based schemes. This is done in the same way; the equivalence between the depth-integrated momentum balance of (9) and the depth-averaged momentum equation of (1b) can be shown using the mass balance in (1a).

First we introduce the following definition for a depth $\bar{h}_f$ at the face that differs from the depth $\tilde{h}_f$ defined in (29). It uses the weighting of the advection term for both the water surface and the bed level:

$$\bar{h}_f=\alpha_f^{c_\mathrm{L}}h_{c_\mathrm{L}}+\alpha_f^{c_\mathrm{R}}h_{c_\mathrm{R}} \tag{30}$$

DOI: 10.1002/fld

This defines the relation between u_f and $q_f = \bar{h}_f u_f$. The time derivative of q_f can now be split into a contribution from the change in water volume and a contribution from the change in velocity:

$$\begin{aligned}\frac{\mathrm{d}q_f}{\mathrm{d}t} &= \alpha_f^{c_\mathrm{L}} \frac{\mathrm{d}h_{c_\mathrm{L}}}{\mathrm{d}t} u_f + \alpha_f^{c_\mathrm{R}} \frac{\mathrm{d}h_{c_\mathrm{R}}}{\mathrm{d}t} u_f + \bar{h}_f \frac{\mathrm{d}u_f}{\mathrm{d}t} \\ &= -\alpha_f^{c_\mathrm{L}} \frac{\sum_k^{c_\mathrm{L}} \pm_k^{c_\mathrm{L}} Q_k}{A_{c_\mathrm{L}}} u_f - \alpha_f^{c_\mathrm{R}} \frac{\sum_k^{c_\mathrm{R}} \pm_k^{c_\mathrm{R}} Q_k}{A_{c_\mathrm{L}}} u_f + \bar{h}_f \frac{\mathrm{d}u_f}{\mathrm{d}t}\end{aligned} \tag{31}$$

where in the last line we have substituted the discretized mass balance (2) and the summations are over the faces k of the left and right cells with fluxes:

$$Q_k = l_k {}^*h_k u_k \tag{32}$$

Using the same fluxes, we make the following choice for the cell-based advection terms:

$$\mathbf{a}_c = \frac{\sum_k^c \pm_k^c Q_k {}^*\mathbf{u}_k}{A_c} \tag{33}$$

where ${}^*\mathbf{u}_k$ is a full vector reconstruction of the velocity at face k. It is reconstructed out of the velocity components from the cell upwind of face k. For Perot's scheme we use the velocity reconstruction as in (16), i.e. we reconstruct the velocity out of the three faces, including face k, of the upwind triangle. For Wenneker's scheme we use only the other two velocity components and not face k itself and reconstruct the unique vector that corresponds with those two components.

Substituting (31) and our choice for the advection terms, we arrive at the following scheme:

$$\begin{aligned}&\bar{h}_f \frac{\mathrm{d}u_f}{\mathrm{d}t} + \alpha_f^{c_\mathrm{L}} \frac{\sum_k^{c_\mathrm{L}} \pm_k^{c_\mathrm{L}} Q_k ({}^*\mathbf{u}_k \cdot \mathbf{n}_f - u_f)}{A_{c_\mathrm{L}}} \\ &\quad + \alpha_f^{c_\mathrm{R}} \frac{\sum_k^{c_\mathrm{R}} \pm_k^{c_\mathrm{R}} Q_k ({}^*\mathbf{u}_k \cdot \mathbf{n}_f - u_f)}{A_{c_\mathrm{R}}} + g\tilde{h}_f \frac{\zeta_{c_\mathrm{R}} - \zeta_{c_\mathrm{L}}}{\Delta x_f} = 0\end{aligned} \tag{34}$$

For both schemes, we can now show that the outgoing fluxes, i.e. $\pm_k^c Q_k > 0$, can be omitted without changing the local momentum balance. For Perot's scheme, this will be deferred to Appendix A. For Wenneker's scheme this is straightforward; for outgoing fluxes one of the two upwind faces is the central face f itself. Thus for the projection of the vector reconstructed out of the two upwind velocity components in the normal direction of face f, we have ${}^*\mathbf{u}_k \cdot \mathbf{n}_f = u_f$. Furthermore, in adding the left and right advection contributions the flux through face f itself out of the upwind cell cancels against the flux going into the downwind cell.

Finally, the u-based scheme that we arrive at is given by

$$\begin{aligned}&\frac{\mathrm{d}u_f}{\mathrm{d}t} + \frac{\alpha_f^{c_\mathrm{L}}}{\bar{h}_f A_{c_\mathrm{L}}} \sum_{\substack{k \\ \text{cell} \\ \text{faces}}}^{\substack{\text{fluxes} \\ \text{into } c_\mathrm{L}}} \pm_k^{c_\mathrm{L}} Q_k ({}^*\mathbf{u}_k \cdot \mathbf{n}_f - u_f) \\ &\quad + \frac{\alpha_f^{c_\mathrm{R}}}{\bar{h}_f A_{c_\mathrm{R}}} \sum_{\substack{k \\ \text{cell} \\ \text{faces}}}^{\substack{\text{fluxes} \\ \text{into } c_\mathrm{R}}} \pm_k^{c_\mathrm{R}} Q_k ({}^*\mathbf{u}_k \cdot \mathbf{n}_f - u_f) + g \frac{\tilde{h}_f}{\bar{h}_f} \frac{\zeta_{c_\mathrm{R}} - \zeta_{c_\mathrm{L}}}{\Delta x_f} = 0\end{aligned} \tag{35}$$

DOI: 10.1002/fld

where for Wenneker's scheme we need only to consider the incoming fluxes for the four faces around the control area of the two combined triangles; for Perot's scheme we include the incoming flux through face f going into the downstream cell.

4.5. *Cartesian scheme*

The Cartesian scheme presented in [1] is based on the same conservation principles. Also for this scheme one can show the equivalence with a depth-integrated momentum balance. The local momentum balance for a face is applied to half of the two adjacent square cells. This is in fact equal to Perot's control volume between the two circumcentres. Unlike the unstructured case, momentum conservation follows directly from the local balances in the two independent covers of the domain with control areas for both momentum components.

Let $u_{i+1/2,j}$ be the velocity in the x-direction stored in the centre of the face between cell (i, j) and $(i+1, j)$. The momentum stored in the control area of length Δx (the distance between the cell centres) and width Δy is given by

$$\Delta x \Delta y \bar{h}_{i+1/2,j} u_{i+1/2,j} \quad \text{with } \bar{h}_{i+1/2,j} = \tfrac{1}{2} h_{i,j} + \tfrac{1}{2} h_{i+1,j} \tag{36}$$

The flux through the left side of this control volume is obtained by averaging the fluxes through the faces at $(i-\frac{1}{2}, j)$ and $(i+\frac{1}{2}, j)$

$$\Delta y \bar{q}_{i,j} = \tfrac{1}{2} Q_{i,j-1/2} + \tfrac{1}{2} Q_{i+1,j-1/2} \tag{37}$$

and similarly for the flux $\Delta y \bar{q}_{i+1,j}$ through the right side of the control volume and the fluxes $\Delta x q_{i+1/2,j-1/2}$ and $\Delta x q_{i+1/2,j+1/2}$ through the bottom and top of the control volume. The advected velocity that is transported with these fluxes in the advection term is again the velocity component stored in the upwind control volume (Figure 4). Following the same procedure as in the previous

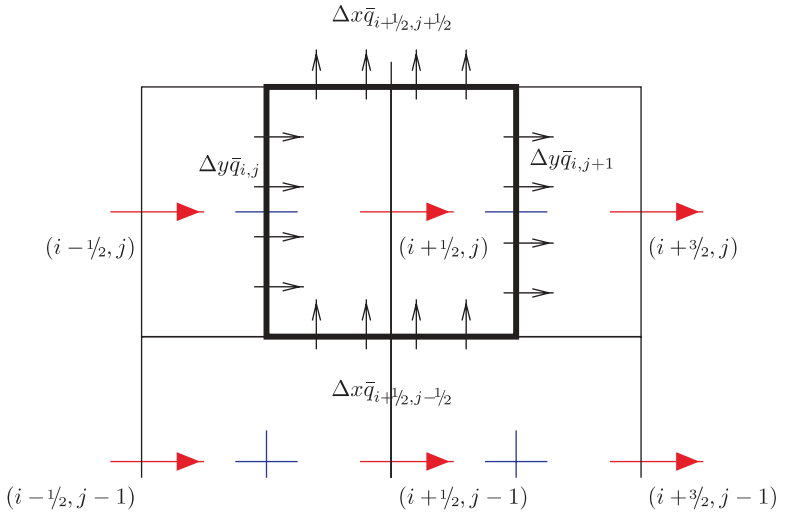

Figure 4. Control volume around face $(i+\frac{1}{2}, j)$ consisting of half of cell (i, j) and half of $(i+1, j)$. Indicated are the fluxes assuming positive flow directions.

DOI: 10.1002/fld

section we can derive a u-based scheme in which the outgoing fluxes have disappeared. Assuming positive flow direction in both the x- and y-directions, i.e. $\bar{q}_{i+1,j}>0$ and $\bar{q}_{i+1/2,j+1/2}>0$ are outgoing fluxes, the scheme after time integration with the θ-scheme looks like:

$$\frac{u^{n+1}_{i+1/2,j}-u^{n}_{i+1/2,j}}{\Delta t}+\frac{\bar{q}^{n}_{i,j}}{\bar{h}^{n}_{i+1/2,j}}\frac{u^{n}_{i+1/2,j}-u^{n}_{i-1/2,j}}{\Delta x}+\frac{\bar{q}^{n}_{i+1/2,j-1/2}}{\bar{h}^{n}_{i+1/2,j}}\frac{u^{n}_{i+1/2,j}-u^{n}_{i+1/2,j-1}}{\Delta y}$$
$$+g\frac{\zeta^{n+\theta}_{i+1,j}-\zeta^{n+\theta}_{i,j}}{\Delta x}=0 \tag{38}$$

This is the same as Equation (24) in [1]. Note that although the scheme applies the same control volumes as Perot's scheme, the schemes are not the same, as in the Cartesian case we do not need a complicated velocity reconstruction for the advected velocity component.

4.6. Constant energy head

As discussed in the previous section, there are certain cases in the modelling of rapidly varied flows where a strict application of the depth-integrated momentum balance leads to physically incorrect solutions and where it is better to look at the energy head H, defined in (13). This is not a quantity that is conserved in a local balance, but for steady flows it should remain constant along a streamline. In semi-Lagrangian schemes, this can be implemented straightforwardly using the reconstructed streamline.

With some basic assumptions the same can be achieved with only a small modification of the momentum conservative scheme. As we are firstly interested in constant energy solutions for steady flows, we need only to consider the balance between the advection term and the hydrostatic pressure term. For one-dimensional flows the discretized balance, transformed in the same way as before to a momentum equation with depth-averaged velocities, reads

$$\frac{q_{\text{in}}}{\bar{h}}\frac{u-{}^{*}u}{\Delta x}+g\frac{\zeta_{\text{R}}-\zeta_{\text{L}}}{\Delta x}=0 \tag{39}$$

We consider a sudden raise in the bottom level at the face between the water level point ζ_{L} and ζ_{R}. The flux coming from the left of the obstacle is determined by the upstream water depth h_{L}. Considering a water depth at the face as in (3), the flux coming over the obstacle is determined by h_{R}. Thus for a steady flow we have

$$q_{\text{in}}=h_{\text{L}}{}^{*}u=q_{\text{out}}\approx h_{\text{R}}u \tag{40}$$

Subsequently we introduce a factor $\bar{h}(h_{\text{L}}+h_{\text{R}})/(2h_{\text{L}}h_{\text{R}})$ in front of the advection term. Working out the new advection term, we obtain

$$\begin{aligned}\frac{\bar{h}(h_{\text{L}}+h_{\text{R}})}{2h_{\text{L}}h_{\text{R}}}\frac{q}{\bar{h}}\frac{u-{}^{*}u}{\Delta x}&=q\left(\frac{1}{2h_{\text{L}}}+\frac{1}{2h_{\text{R}}}\right)\frac{u-{}^{*}u}{\Delta x}\\&=\frac{1}{2}({}^{*}u+u)\frac{u-{}^{*}u}{\Delta x}\\&=\frac{1}{2}\frac{u^2-{}^{*}u^2}{\Delta x}\end{aligned} \tag{41}$$

DOI: 10.1002/fld

With this advection term it can be easily seen that the energy head is conserved across the obstacle

$$gh_{\mathrm{L}}+\tfrac{1}{2}{}^{*}u^2=gh_{\mathrm{R}}+\tfrac{1}{2}u^2 \tag{42}$$

Note that the factor is consistent with 1 for smooth geometries, so that the scheme is still consistent away from the jump, only at the jump itself the scheme is no longer momentum conservative. To avoid division by zero it is in fact better to put the inverse of the factor in front of the pressure gradient term. In many situations the two-dimensional flow over a sudden bottom elevation, e.g. the flow over a dike or over a weir, will be almost perpendicular to the elevation. In this case the factor in front of the pressure gradient can also be applied to obtain constant energy solutions across the elevation. The factor can easily be implemented as a switch that is only applied for strong contractions in the direction of the flow. For the rest of the domain, the momentum conservative scheme remains unmodified.

5. CARLSON'S SCHEME

The advection scheme applied in (38) can be rewritten as a three-point interpolation

$$u^{n+1}=(1-c_x-c_y)u^n+c_xu_x^n+c_yu_y^n \tag{43}$$

with the shorthand

$$u^n=u^n_{i+1/2,j},\quad u_x^n=u^n_{i-1/2,j},\quad u_y^n=u^n_{i+1/2,j-1} \tag{44}$$

and dimension-less constants c_x and c_y, acting as Courant numbers

$$c_x=\left(\frac{\bar{q}^n_{i,j}}{\bar{h}^n_{i+1/2,j}}\right)\frac{\Delta t}{\Delta x},\quad c_y=\left(\frac{\bar{q}^n_{i+1/2,j-1/2}}{\bar{h}^n_{i+1/2,j}}\right)\frac{\Delta t}{\Delta x} \tag{45}$$

This is only stable within the triangle u, u_x and u_y. That is for

$$c_x\geqslant 0,\quad c_y\geqslant 0\quad\text{and}\quad c_x+c_y\leqslant 1 \tag{46}$$

The positivity of c_x and c_y is already implied by the fact that they represent incoming fluxes. The last condition, however, may put a rather strict constraint on the time step.

The one-dimensional scheme, say $c_y=0$, is stable only if $0\leqslant c_x\leqslant 1$, that is, if we interpolate in a point between u^n and u_x^n. This is in the point where the characteristic intersects the $t=t^n$-line in the (x,t)-timenet (see Figure 5). If we interpolate at the first intersection with the lines of the timenet, then for $c_x>1$ we obtain an interpolation between u_x^n and u_x^{n+1}. This gives the following scheme:

$$u^{n+1}=\begin{cases}(1-c_x)u^n+c_xu_x^n, & 0\leqslant c_x\leqslant 1\\ \left(1-\dfrac{1}{c_x}\right)u_x^{n+1}+\dfrac{1}{c_x}u_x^n, & c_x>1\end{cases} \tag{47}$$

This scheme is also applied in Carlson's S_n-method [15], see also [16, 17]. A more recent application to a Godunov-type scheme can be found in [18, 19]. The scheme is only locally implicit. This has

DOI: 10.1002/fld

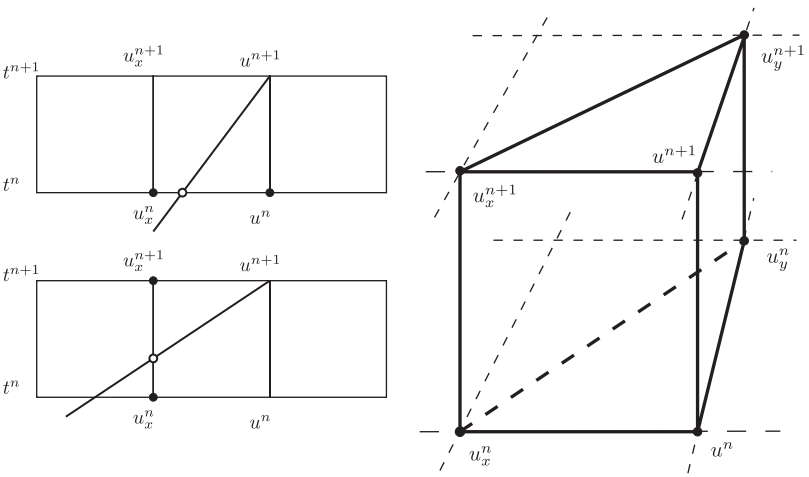

Figure 5. In the one-dimensional case, Carlson's scheme switches between an explicit interpolation between u^n and u_x^n (top left figure) and an implicit interpolation between u_x^{n+1} and u_x^n (bottom left figure). In the two-dimensional case it switches between an explicit interpolation in the triangle u^n, u_x^n and u_y^n and an implicit bilinear interpolation in the square $u_x^{n+1}, u_y^{n+1}, u_x^n$ and u_y^n.

the advantage that the equations can be solved much faster if only the Courant violation occurs very locally, near sharp gradients or in small cells. The explicit values are calculated directly, whereas the implicit equations can be solved with just one sweep in each direction.

For a generalization to two dimensions, we rewrite the scheme as

$$u^{n+1}-u^n+(1-\theta(c_x))\cdot c_x(u^n-u_x^n)+\theta(c_x)\cdot c_x(u^{n+1}-u_x^{n+1})=0 \tag{48}$$

with a varying θ

$$\theta(c)=\max\left(0,1-\frac{1}{c}\right) \tag{49}$$

If we apply this varying-θ scheme, using $\theta(c_x+c_y)$, for the two-dimensional case and collect all u^{n+1}-terms on the left-hand side, we obtain

$$u^{n+1}=\begin{cases}(1-c_x-c_y)u^n+c_xu_x^n+c_yu_y^n, & c_x,c_y\geqslant 0 \text{ and } c_x+c_y\leqslant 1\\ \left(1-\dfrac{1}{c_x+c_y}\right)\left(\dfrac{c_x}{c_x+c_y}u_x^{n+1}+\dfrac{c_y}{c_x+c_y}u_y^{n+1}\right) & \\ \quad+\left(\dfrac{1}{c_x+c_y}\right)\left(\dfrac{c_x}{c_x+c_y}u_x^n+\dfrac{c_y}{c_x+c_y}u_y^n\right), & c_x,c_y\geqslant 0 \text{ and } c_x+c_y>1\end{cases}$$

For $c_x+c_y>1$ we obtain a bilinear interpolation between u_x^n, u_x^{n+1}, u_y^n and u_y^{n+1} in the intersection of the characteristic with the plane spanned by those four points. Hence, the scheme prescribes an interpolation in the point where the characteristic leaves the space–time prism (Figure 5). If

DOI: 10.1002/fld

$c_x+c_y>1$ but $c_y\leqslant 1$, then we can also use the 3-point interpolation

$$u^{n+1}=\left(1-\frac{1}{c_x+c_y}\right)u_x^{n+1}+\left(\frac{1-c_y}{c_x+c_y}\right)u_x^n+\left(\frac{c_y}{c_x+c_y}\right)u_y^n \tag{50}$$

and similarly for $c_x+c_y>1$ and $c_x\leqslant 1$. This has the advantage of having a smaller implicit stencil, leading to faster convergence of the sweeping algorithm.

Also the general unstructured scheme (35) can be expressed as an interpolation

$$u_f^{n+1}=(1-c_{\text{sum}})u_f^n+\sum_{\substack{k\\ \text{faces}}}^{\text{incoming}} c_k\,{}^*\mathbf{u}_k\cdot\mathbf{n}_f \tag{51}$$

where the summation is over faces with incoming flux, ${}^*\mathbf{u}_k$ are the full velocity vectors reconstructed at these faces, c_k are dimensionless coefficients and c_{sum} is the sum of these:

$$c_k=\Delta t\,\frac{-\alpha_f^{\text{L/R}}\pm_{c_{\text{L/R}}}^k Q_k}{\bar{h}_f A_{c_{\text{L/R}}}},\quad c_{\text{sum}}=\sum_{\substack{k\\ \text{faces}}}^{\text{incoming}} c_k \tag{52}$$

This is again stable if all $c_k\geqslant 0$ (this is true because only incoming fluxes contribute) and $c_{\text{sum}}\leqslant 1$. For Perot's scheme, f is itself one of the faces k with incoming flux. ${}^*\mathbf{u}_f$ in the corresponding term is itself dependent on u_f^n. In Appendix A it is explained, however, how we can rewrite into an interpolation in which the total contribution from u_f^n is given explicitly.

An unconditionally stable scheme can be derived using the varying $\theta(c_{\text{sum}})$-scheme

$$u_f^{n+1}=\begin{cases}(1-c_{\text{sum}})u_f^n+\sum_k c_k\,{}^*\mathbf{u}_k^n\cdot\mathbf{n}_f, & c_k\geqslant 0 \text{ and } c_{\text{sum}}\leqslant 1\\ \left(1-\dfrac{1}{c_{\text{sum}}}\right)\left(\sum_k \dfrac{c_k}{c_{\text{sum}}}\,{}^*\mathbf{u}_k^{n+1}\cdot\mathbf{n}_f\right) & \\ \quad+\dfrac{1}{c_{\text{sum}}}\left(\sum_k \dfrac{c_k}{c_{\text{sum}}}\,{}^*\mathbf{u}_k^n\cdot\mathbf{n}_f\right) & c_k\geqslant 0 \text{ and } c_{\text{sum}}>1\end{cases}$$

The locally implicit advection scheme can be combined with the semi-implicit scheme of Section 2 by introducing a fractional step. In the first step, the implicit equations of the advection scheme are solved with a sweeping algorithm. The calculated advected velocities are then used as starting point for the second step in which the rest of the terms are integrated using the semi-implicit scheme. The use of a fractional step introduces a first-order time error but only for the few velocities for which the advection is calculated implicitly.

6. MODIFIED CUT-CELL TECHNIQUE CREATING ORTHOGONAL GRIDS

Unstructured grids greatly improve the possibilities of dealing with complex flow domains. Most two-dimensional unstructured grid techniques are based on triangular grids. Taking the circumcentre as the centre of each cell, a triangular grid without any obtuse triangles meets the requirement of an unstructured orthogonal grid. For obtuse triangles, however, the circumcentres lie outside the cell, and in this case the face between two cells no longer lies between the two corresponding centres causing inaccuracy and instability in the pressure gradient calculation.

DOI: 10.1002/fld

The generation of non-obtuse grids is far from trivial. Many algorithms are based on Delaunay triangulations [20] and only provide lower bounds on the smallest angle found in the triangles. Some non-obtuse triangulation algorithms are known [21, 22], but it is yet unclear whether they can be combined with other quality criteria and provide enough flexibility for local refinements. Even in non-obtuse triangulations, the circumcentres may come arbitrarily close together or even coincide. Acute triangulations [23, 24], i.e. triangulations with all angles strictly smaller than 90°, are even harder to generate.

A disadvantage of finite volume methods on unstructured grids in general is the difficulty to derive higher-order schemes. Especially in the case of unstructured staggered grids where only arbitrary components of the velocity on arbitrary locations are given, it is difficult to reconstruct a higher-order interpolation of the velocity field.

The *Cartesian cut-cell technique* is another grid technique to deal with complex boundaries (see [25] for an overview or [26, 27] for applications to shallow water flows). One starts with an ordinary Cartesian grid. The boundary is represented by a line segment in each cell that simply cuts off the boundary cell. On the Cartesian cells in the interior, all standard numerical schemes available for structured grids, including higher-order methods, can be applied. The cut-off cells, however, need a special treatment, as their areas and the widths of their faces need to be corrected. A common problem with this method is the occurrence of small triangles, which strains the CFL-condition.

A specific problem for schemes with the orthogonality requirement is the fact that the original cell centres of the cut cells, after cutting off the boundary, may end up outside the domain. The centres can be moved but then the grid is no longer orthogonal, and the calculation of the pressure gradient needs to be modified. Our approach aims at restoring orthogonality by a further sub-division of the cut cells.

Cutting off a boundary with a straight line divides the rectangular Cartesian cells in triangles, quadrilaterals or pentagons. The resulting triangles are always orthogonal. This means that its circumcentre lies exactly on the boundary segment. The cut-off quadrilaterals have two right angles. There is always one way of dividing those in two non-obtuse triangles (Figure 6).

For the pentagons in most cases it is possible to draw a line segment perpendicular to and starting at the boundary face to the vertex opposite of this face. This divides the pentagon in two quadrilaterals in which one can find centres that meet the orthogonality requirement for all three interior faces. In cases in which such a line segment perpendicular to the boundary face cannot be found, it is also not possible to divide the pentagon in three acute triangles. An acute triangulation exists [24] but may lead to excessively small triangles. If we drop the orthogonality requirement

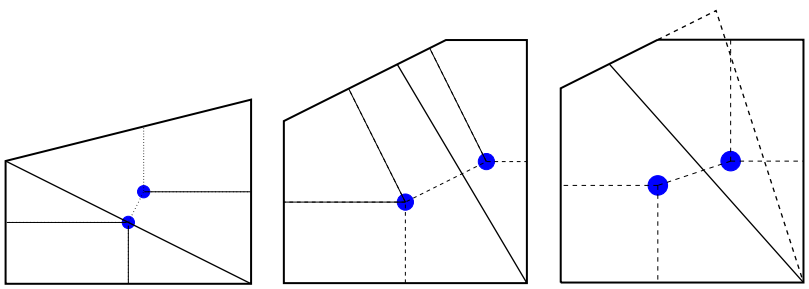

Figure 6. Quadrilateral divided into two triangles. Pentagon divided into two quadrilaterals (in the right one it is not possible to find an orthogonal solution).

DOI: 10.1002/fld

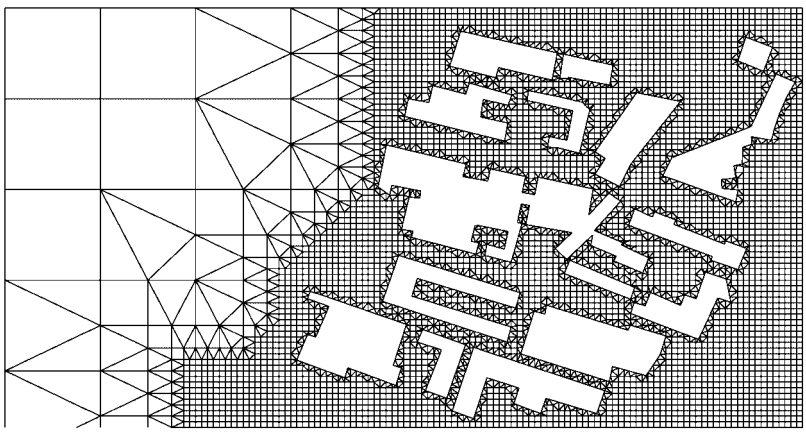

Figure 7. Example of cut-cell grid with quadtree refinement.

and divide the pentagon with a line segment between the middle of the boundary face and the opposite vertex, the pressure gradient on this new face can still be calculated using information of the boundary condition. For instance for a closed boundary, the pressure gradient should be parallel to the boundary. This is the same direction as the vector between the two cell centres. Hence, the complete pressure gradient vector can be calculated out of the pressure difference in the centres and projected into the face normal direction. Thus, we preserve the symmetry and positive definiteness of the linear system.

This technique provides a very efficient way of generating a grid that very accurately approximates the boundaries. In many inundation calculations, obstacles such as large buildings occur. They create holes in the flow domain, that are in general difficult to incorporate in the grid using other techniques. The fact that the grid remains Cartesian in the interior makes it possible to apply higher-order methods there. The problem with small triangles can be solved using the locally implicit scheme described in the previous section. Grid refinement can be implemented using quadtree refinement of the Cartesian grid in combination with some extra triangles in the transition areas to maintain orthogonality (see Figure 7).

7. TEST CASES

7.1. One-dimensional flow in an oblique channel

Very simple but relevant tests can be performed by studying one-dimensional flows in a straight channel that has been rotated with respect to the Cartesian-grid orientation. The channel is approximated with a cut-cell grid (see Figure 9). In this domain one can compare several problems for which the analytical solution is known with the numerical result. Moreover, we can compare with the result for a Cartesian staircase approximation of the channel.

7.1.1. Hydraulic jump after sill. This example is a steady-state problem for a channel of 100 m rotated under an angle of 37°. In the middle of the channel, there is a sill with a crest of 1 m height and a length of 10 m. The slopes have a tangent of 0.2. At inflow a depth-integrated velocity

DOI: 10.1002/fld

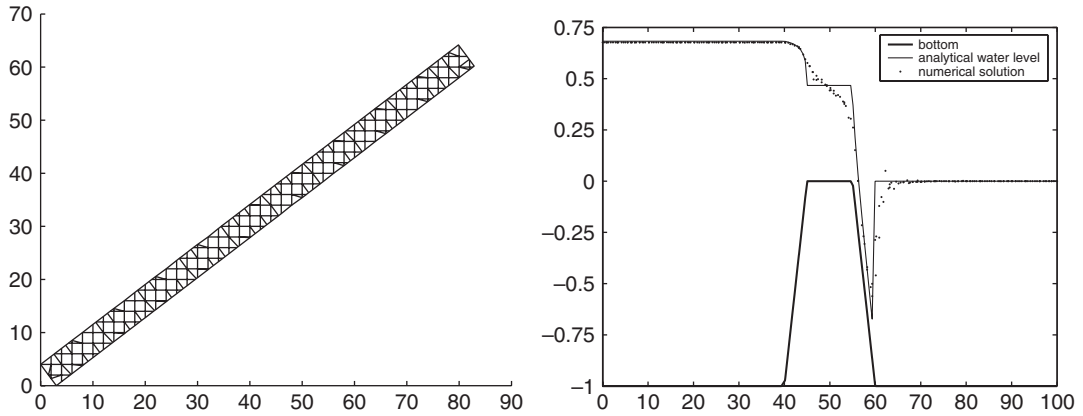

Figure 8. Numerical result of hydraulic jump after sill on coarse grid of $\Delta x = 2$.

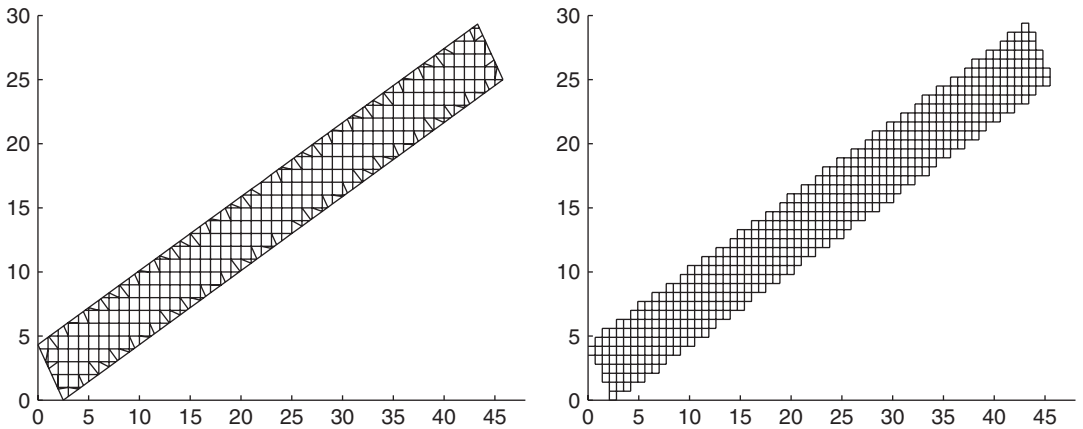

Figure 9. Straight channel under angle of 30° with respect to the grid orientation, approximated with cut-cell grid (left, $\Delta x = 1$) and Cartesian grid (right, $\Delta x = 0.7$).

of $1\,\mathrm{m}^2/\mathrm{s}$ is prescribed and the downstream water level is kept at 1 m. Downstream of the sill, a hydraulic jump will occur. For this problem, a cut-cell grid with Cartesian cells of 2 m is employed. The smallest cell in the grid has an area of $0.01\,\mathrm{m}^2$, even smaller cells were removed (Figure 8).

Comparing the numerical results of the scheme with the analytical solution, some first-order errors are visible near the shock above the crest. Better results could be achieved implementing more accurate fluxes for the divergence and advective terms of the scheme combined with flux limiters. The main flow characteristics (upstream water level, location and depth of the jump), however, are accurately represented using only a few cells to represent the steep bottom rise. This makes the scheme highly effective in flooding situations where various steep bottom features need to be incorporated using as little resolution as possible.

If the jump velocities of $5.2\,\mathrm{ms}^{-1}$ occur; high Courant numbers can be expected especially for the smaller cells. In Table I, however, it is shown that even for larger time steps we obtain accurate

DOI: 10.1002/fld

Table I. Numerical results for hydraulic jump after sill with different time steps.

Δt	Implicit equations	Iterations	Upstream error
0.01	0	1	0.0056
0.1	2	2	0.0060
0.2	8	3	0.0068
0.5	39	7	0.0077
1.0	95	15	0.0093
2.0	275	20	0.0470
5.0	386	34	0.1652
10	387	39	0.2772

The number of implicit equations is equal to the number of faces at which the Courant number is greater than 1. Also shown is the number of Gauss–Seidel iterations needed to solve the equations and the error in the upstream water level.

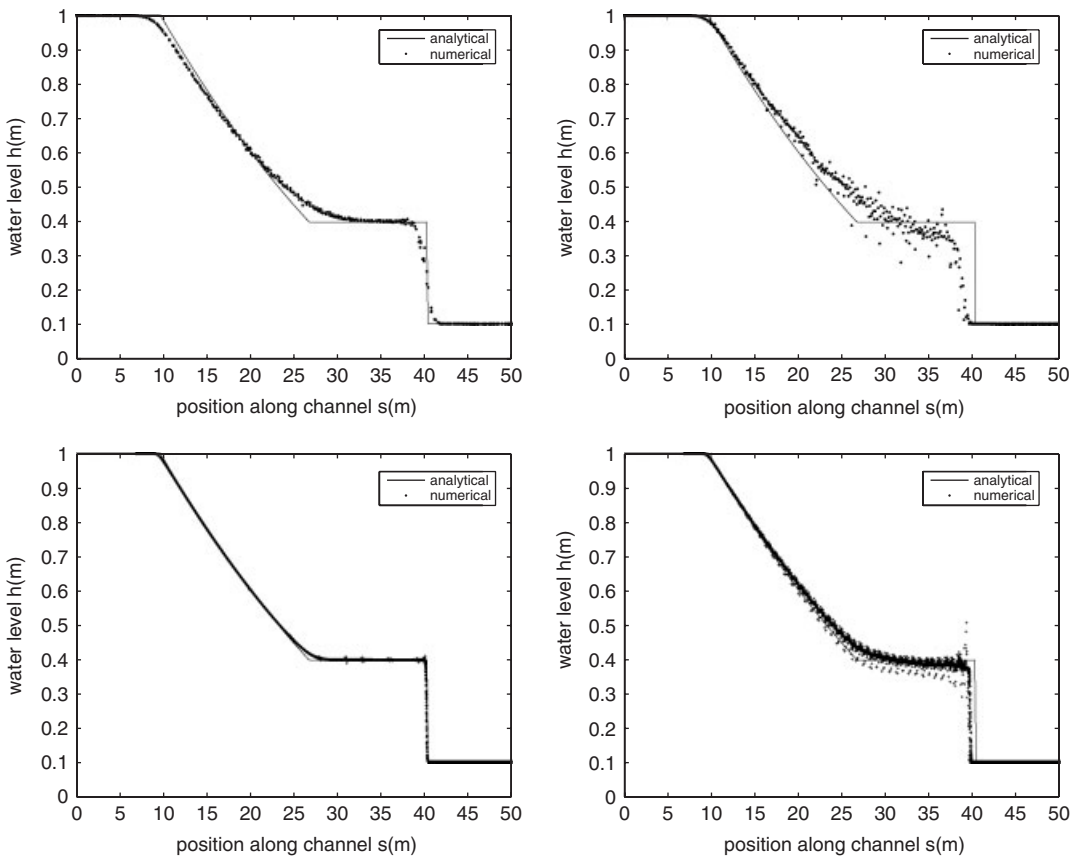

Figure 10. Dam break over wet bed. Numerical results (dots) compared with analytical solution (straight line). Top left: cut-cell grid, $\Delta x = 1$; top right: Cartesian grid, $\Delta x = 0.7$; bottom left and right: cut-cell and Cartesian grids, $\Delta x = 0.1$.

DOI: 10.1002/fld

results. This is achieved using the locally implicit time integration of Section 5. From the table we can read that as long as the number of Courant violations is small, the required extra work is limited.

7.1.2. Dam break over wet bed. A dam break is calculated in a channel of 50 m rotated under an angle of 30°. The upstream water level is 1 m and the wet bed level downstream is at 0.1 m. At $t=0$ the shock starts at $x=25$ with zero initial velocity. Shown is the numerical solution after 5 s. Already on a relatively coarse cut-cell grid good results are achieved, with a correct shock speed and height of the bore. On a Cartesian staircase grid with slightly more cells (both grids are given in Figure 9), the results are considerably worse. On a finer cut-cell grid, the numerical solution converges to the analytical solution, whereas the numerical solution on a Cartesian staircase grid, again with roughly the same number of cells, keeps showing distortions near the boundary (Figures 10 and 11).

7.2. Comparison of Perot and Wenneker's schemes

Two variants of the discretization of the momentum balance for unstructured grids have been discussed based on either Perot's or Wenneker's scheme. The advantage of Perot's scheme is that its conservation properties can be proven in a rigorous way. A disadvantage is that because the weighting of the left and right cells contribution to the advection at the face is based on the distance between circumcentres and faces, the weighting factors become negative in the case of circumcentres that lie outside the cell. This leads to instabilities in the scheme. For Wenneker's scheme, although circumcentres outside of their cells may hamper the accuracy, this does not have a direct consequence for the stability of the scheme.

As we have seen it is not straightforward to generate grids with all circumcentres strictly within the cell. The modified cut-cell technique introduced in the previous section provides a mechanism to generate such grids. Because the grid is mostly Cartesian in the interior, this does not provide a good comparison between the unstructured schemes based on Perot and Wenneker. In fact the tests of the previous section that uses Wenneker's scheme near the boundary hardly show any difference using Perot's scheme. A better comparison can be performed on a triangular grid in which all triangles are acute to avoid instabilities for Perot's scheme. The same tests of the previous section in a rectangular channel have been performed this time with an acute triangulation of which a part is shown in Figure 12. The results are shown in Table II. As we can see the scheme based on Perot's scheme performs better for the hydraulic jump and the dam break with wet bed, whereas Wenneker's scheme performs slightly better for the dam break with dry bed. In general the observed differences between the two schemes were small. Because of the practical restrictions for the grid of the Perot scheme, all other tests in this section have been performed using Wenneker's scheme for advection.

7.3. Oblique hydraulic jump

The oblique hydraulic jump, which occurs in supercritical flow in converging channels, is a well-known test case for shock-capturing schemes [8, 28]. It gives a clear example of the ease of use the proposed cut-cell technique. Upstream supercritical boundary conditions of $h=1\,\mathrm{m}$ and $u=8.57\,\mathrm{ms}^{-1}$ are given for a domain with a converging wall under an angle of 8.95° with the incoming stream. This creates an oblique hydraulic jump, for which the angle with the upstream flow of 30°, and the water level $h=1.5\,\mathrm{m}$ and velocity $u=7.96\,\mathrm{ms}^{-1}$ downstream of the jump can

DOI: 10.1002/fld

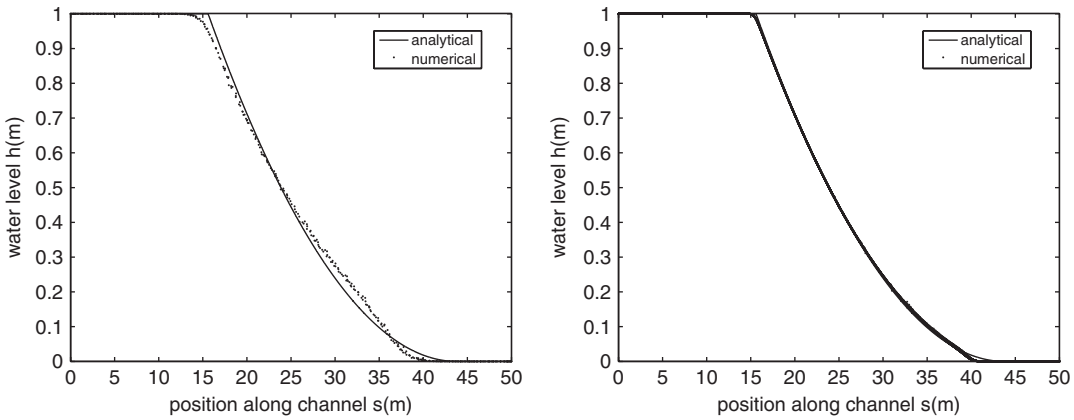

Figure 11. Dam break over dry bed. Numerical results (dots) compared with analytical solution (straight line). Left: cut-cell grid, $\Delta x = 1$; right: cut-cell grid, $\Delta x = 0.1$.

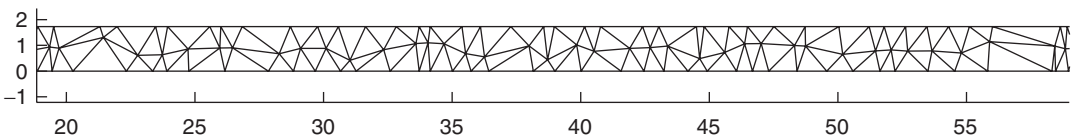

Figure 12. Part of the grid on which comparisons between Perot's and Wenneker's schemes were performed.

Table II. Comparison numerical results using Perot's or Wenneker's scheme.

	Perot's scheme	Wenneker's scheme
Upstream error hydraulic jump	0.0028	0.0089
L2-error dam break over wet bed after 8 s	0.2555	0.3116
L2-error dam break over wet bed after 15 s	0.2154	0.3138
L2-error dam break over dry bed after 4 s	0.1645	0.1438
L2-error dam break over dry bed after 8 s	0.1551	0.1240

be derived analytically [29]. Shown in Figure 13 are the results for the scheme as described in this paper. Similar to the one-dimensional hydraulic jump after a sill described before, the results show a typical first-order approximation of the shock. This also leads to slightly higher velocities after the shock 7.99–8.03 ms^{-1}, but again the main flow features are accurately represented—a water level of $h = 1.499$ m, and the shock angle can be seen in Figure 13 to be very close to the predicted 30°.

7.4. River bend flow

A clear example of the error introduced by staircase-like boundaries can be seen in the modelling of the flow in a river bend. We study a U-shaped flume with centreline radius of 4.25 m and with 6.00 m long straight tangent reaches (Figure 14). Measurements and computational results,

DOI: 10.1002/fld

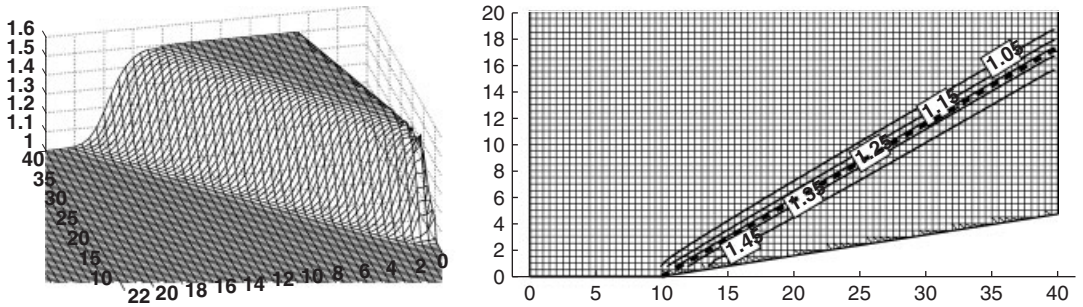

Figure 13. Oblique hydraulic jump. In the right figure the water level contour lines of the numerical solution are drawn. The dashed line indicates the shock position according to the analytical solution.

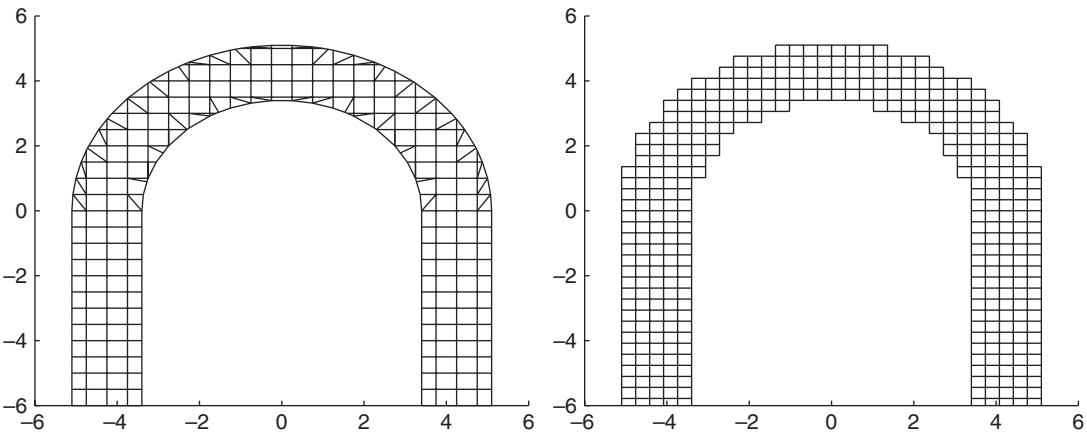

Figure 14. Example of cut-cell grid (left, $\Delta x = 0.5\,\mathrm{m}$) and Cartesian grid (right, $\Delta x = 0.34\,\mathrm{m}$) of U-shaped flume.

using curvilinear coordinates and stationary equations, can be found in [30]. The computational results are used as a reference and compared with the numerical results on a cut-cell grid and a pure Cartesian grid of ± 4500 cells (see Figure 15). The applied bottom roughness with Chezy $C = 57\,\mathrm{m}^{1/2}/\mathrm{s}$ causes a 10% elevation of the water surface upstream. This is reproduced accurately by the cut-cell computation. The pure Cartesian computation, however, shows an elevation of 26.7% which indicates a large energy loss caused by artificial boundary effects.

7.5. Circular dam break

The circular dam break [7] provides an interesting two-dimensional test case for which the exact solutions can be analysed by projection in the radial direction. A cylinder of water with an initial height of 2.5 m is released in a surrounding domain with initial water height of 0.5 m. The results are analysed before the diverging bore reaches the closed boundaries of the domain. For this case the scheme of this paper was tested on a completely triangular mesh. In Figure 16 the results are compared with those on a structured mesh. It can be seen that the results are very similar. Both

DOI: 10.1002/fld

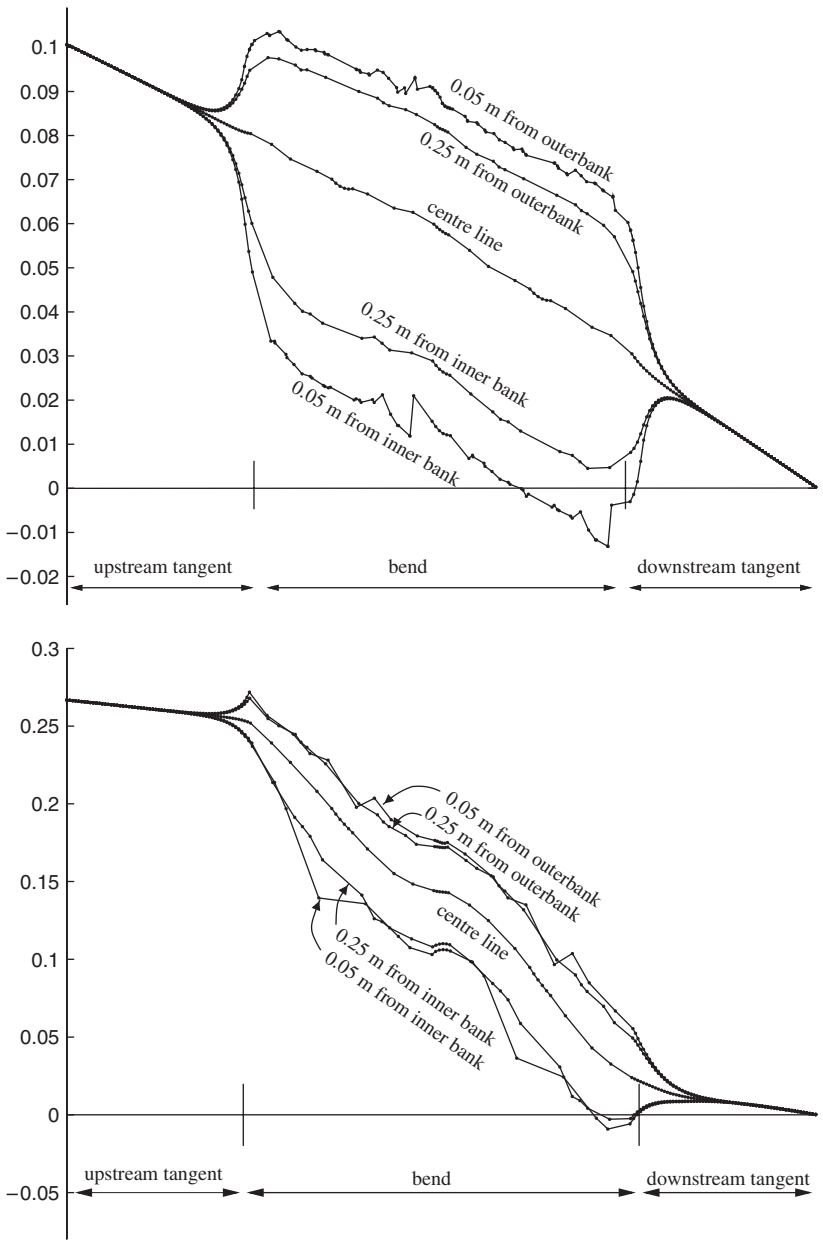

Figure 15. Profile of water height along U-bend. Numerical results on cut-cell grid (top) and Cartesian grid (bottom), both with $\Delta x = 0.1\,\mathrm{m}$. Downstream water depth is $H = 0.18\,\mathrm{m}$. Water heights in these figures are above downstream level and in relative coordinates $h' = h/H$.

DOI: 10.1002/fld

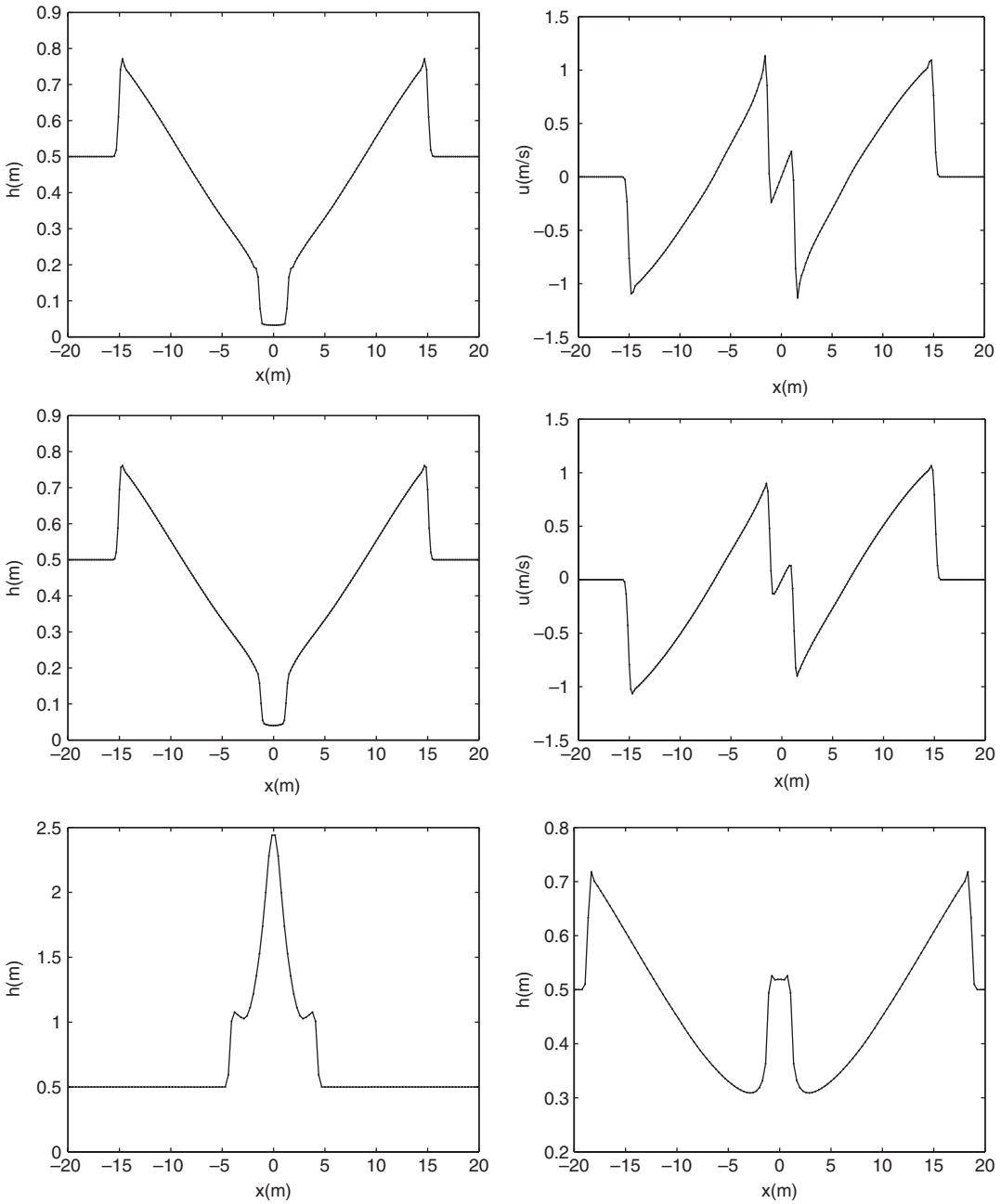

Figure 16. Numerical results of circular dam break test. Profile along $y = 0$-line. Top two figures give water surface and velocity after 3.5 s using Cartesian grid. Middle two figures give the same for a triangular grid. Bottom figures give the water surface using triangular grid at two other times $t = 0.4$ and 4.7 s.

DOI: 10.1002/fld

results accurately represent the semi-analytical radial one-dimensional solution given in [7]. The Cartesian mesh solution gives in fact a slightly better representation at the exact shock location, which is probably due to the fact that the Cartesian mesh is aligned with the cross section along the x-axis that is given in the figure. Shock speeds, and water levels and velocities of the in-between states are, however, very close to the reference solution (errors less than 1%).

8. CONCLUSIONS

A robust and efficient unstructured method for the numerical simulation of rapidly varied flows has been presented. The scheme guarantees mass conservation, non-negative water depths, and provides by choice, based on physical consideration, either momentum conservation or constancy of energy head. Owing to the guarantee for non-negative water depths, no special flooding and drying procedures need to be implemented. The appropriate application of momentum or energy conservation is needed to accurately model the flow near steep bottom gradients and propagating shock waves.

The ability of unstructured grids to accurately represent complex boundaries is especially useful in the complicated geometry of a flooded urban area. To enable an efficient solution of the system of equations, an orthogonality condition has to be put on the grid. This complicates the straightforward application of triangular grids. The hybrid grid approach proposed in this paper offers boundary conformance while respecting the orthogonality condition. The small-cell problem in Cartesian cut-cell approaches can be solved with the locally implicit time integration of Section 5. This scheme also improves the efficiency of the scheme for rapidly varied flows where high velocities may occur very locally.

The efficiency and robustness of the method allow application to large-scale inundation problems. Although more accurate results can be obtained using higher-order methods based on Riemann solvers, and with three-dimensional non-hydrostatic models, the main flow properties of rapidly varied flows, such as jumps and shock speeds, are accurately represented with this scheme, while maintaining efficiency through the semi-implicit staggered approach.

APPENDIX A: ANALYSIS OF THE FLUX TERMS IN PEROT'S SCHEME

To show that in (34) the outgoing fluxes may be omitted without changing the local momentum balance, we need to go back to the cell-based momentum balance. Although the relationship $q_f = \bar{h}_f u_f$ does not imply $\mathbf{q}_c = h_c \mathbf{u}_c$ for the reconstructed cell-based vectors $\mathbf{q}_c$ and $\mathbf{u}_c$, we can derive the following relation:

$$\begin{aligned}\sum_{\text{cells}} A_c \mathbf{q}_c = \sum_{\text{faces}} \Delta x_f l_f q_f \mathbf{n}_f &= \sum_{\text{faces}} (\Delta x_f^{c_L} h_{c_L} + \Delta x_f^{c_R} h_{c_R}) u_f \mathbf{n}_f \\ &= \sum_{\text{cells}} h_c \sum_{\substack{f \\ \text{cell} \\ \text{faces}}} A_f^c u_f \mathbf{n}_f \\ &= \sum_{\text{cells}} A_c h_c \mathbf{u}_c \end{aligned} \tag{A1}$$

DOI: 10.1002/fld

Now for the local acceleration and advection terms in the cell-based momentum balance we can express

$$\sum_{\substack{c\\ \text{cells}}} A_c \frac{\mathrm{d}\mathbf{q}_c}{\mathrm{d}t} + A_c \mathbf{a}_c = \sum_{\substack{c\\ \text{cells}}} \left\{ A_c h_c \frac{\mathrm{d}\mathbf{u}_c}{\mathrm{d}t} + A_c \frac{\mathrm{d}h_c}{\mathrm{d}t} \mathbf{u}_c + \sum_{\substack{f\\ \text{cell}\\ \text{faces}}} \pm_f^c Q_f {}^*\mathbf{u}_f \right\}$$

$$= \sum_{\substack{c\\ \text{cells}}} \left\{ A_c h_c \frac{\mathrm{d}\mathbf{u}_c}{\mathrm{d}t} + \sum_{\substack{f\\ \text{cell}\\ \text{faces}}} \pm_f^c Q_f ({}^*\mathbf{u}_f - \mathbf{u}_c) \right\} \tag{A2}$$

In this form it is clear that the outgoing fluxes $\pm_f^c Q_f > 0$ drop out. Transforming back to a face-based momentum balance this means that in (34) the outgoing flux terms can be dropped without changing the corresponding cell-based momentum balance. Note, however, that the flux through face f itself in (34) does not cancel in adding the left and right advection contribution, as it does in Wenneker's scheme. The upwind incoming velocity ${}^*\mathbf{u}_f$ in the corresponding term depends on u_f itself. Suppose i and j are the other two faces in the upwind cell. For the unique vector $\mathbf{u}_{ij}$ such that $\mathbf{u}_{ij} \cdot \mathbf{n}_i = u_i$ and $\mathbf{u}_{ij} \cdot \mathbf{n}_j = u_j$, we may express (assuming i and j have inward pointing normals)

$$\mathbf{u}_{ij} \cdot \mathbf{n}_f = \frac{l_i u_i + l_j u_j}{l_f} \tag{A3}$$

This follows from considering the divergence of $\mathbf{u}_{ij}$ as a constant over the triangle. Furthermore, in Figure A1 we can see the following identity:

$$\Delta x_i^c \mathbf{n}_i \cdot \mathbf{n}_f = \Delta x_j^c \mathbf{n}_j \cdot \mathbf{n}_f = \frac{A_c - \Delta x_f^c l_f}{l_f} \tag{A4}$$

Therefore in the upwind cell c with faces f, i and j, we can express

$$\begin{aligned} {}^*\mathbf{u}_f \cdot \mathbf{n}_f = \mathbf{u}_c \cdot \mathbf{n}_f &= \frac{\Delta x_f^c l_f u_f + (\Delta x_i^c l_i u_i \mathbf{n}_i + \Delta x_j^c l_j u_j) \cdot \mathbf{n}_f}{A_c} \\ &= \frac{\Delta x_f^c l_f u_f + \mathbf{u}_{ij} \cdot \mathbf{n}_f (A_c - \Delta x_f^c l_f)}{A_c} \\ &= \frac{\Delta x_f^c l_f}{A_c} u_f + \left(1 - \frac{\Delta x_f^c l_f}{A_c}\right) \mathbf{u}_{ij} \cdot \mathbf{n}_f \end{aligned} \tag{A5}$$

This means that in the interpolation of (51) we can explicitly write out the contribution from u_f^n by

$$\begin{aligned} u_f^{n+1} &= (1 - c_s) u_f^n + \sum_{\substack{k \neq f\\ \text{faces}}}^{\text{incoming}} c_k {}^*\mathbf{u}_k \cdot \mathbf{n}_f + c_f \frac{\Delta x_f^c l_f}{A_c} u_f^n + c_f \left(1 - \frac{\Delta x_f^c l_f}{A_c}\right) \mathbf{u}_{ij} \cdot \mathbf{n}_f \\ &= (1 - c_s') u_f^n + \sum_{\substack{k \neq f\\ \text{faces}}}^{\text{incoming}} c_k {}^*\mathbf{u}_k \cdot \mathbf{n}_f + c_{ij} \mathbf{u}_{ij} \cdot \mathbf{n}_f \end{aligned} \tag{A6}$$

DOI: 10.1002/fld

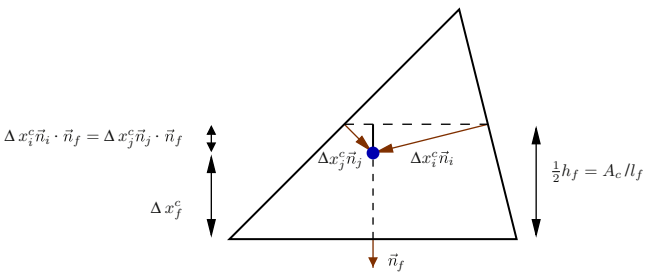

Figure A1. From this triangle with faces f, i and j we can read off Equation (A4).

where c_{ij} and c'_s are given by (note that always: $0 \leqslant \Delta x_f^c l_f \leqslant A_c$)

$$c_{ij} = \left(1 - \frac{\Delta x_f^c l_f}{A_c}\right) c_f, \quad c'_s = \sum_{\substack{\text{incoming} \\ \text{faces}}}{}_{k \neq f} c_k + c_{ij} \tag{A7}$$

The locally implicit scheme is then given by

$$u_f^{n+1} = \begin{cases} (1 - c'_s) u_f^n + \sum_k c_k \, {}^*\mathbf{u}_k^n \cdot \mathbf{n}_f + c_{ij} \mathbf{u}_{ij}^n \cdot \mathbf{n}_f, & c_k \geqslant 0 \text{ and } c'_s \leqslant 1 \\ \left(1 - \dfrac{1}{c'_s}\right) \left(\sum_k \dfrac{c_k}{c'_s} \, {}^*\mathbf{u}_k^{n+1} \cdot \mathbf{n}_f + \dfrac{c_{ij}}{c'_s} \mathbf{u}_{ij}^{n+1} \cdot \mathbf{n}_f \right) & \\ \quad + \dfrac{1}{c'_s} \left(\sum_k \dfrac{c_k}{c'_s} \, {}^*\mathbf{u}_k^n \cdot \mathbf{n}_f + \dfrac{c_{ij}}{c'_s} \mathbf{u}_{ij}^n \cdot \mathbf{n}_f \right), & c_k \geqslant 0 \text{ and } c'_s > 1 \end{cases}$$

REFERENCES

1. Stelling GS, Duinmeijer SPA. A staggered conservative scheme for every Froude number in rapidly varied shallow water flows. *International Journal for Numerical Methods in Fluids* 2003; **43**:1329–1354.
2. Leendertse JJ. Aspects of a computational model for long period water-wave propagation. *Memorandum RM-5294-PR*, RAND Corporation, 1967.
3. Stelling GS. On the construction of computational methods for shallow water flow problems. *Rijkswaterstaat Communication*, vol. 35. Rijkswaterstaat: Dutch, 1984.
4. Casulli V. Semi-implicit finite-difference methods for the 2-dimensional shallow-water equations. *Journal of Computational Physics* 1990; **86**:56–74.
5. Wilders P, van Stijn ThL, Stelling GS, Fokkema GS. A fully implicit splitting method for accurate tidal computations. *International Journal for Numerical Methods in Engineering* 1988; **12**:2707–2721.
6. Ham DA, Kramer SC, Stelling GS, Pietrzak J. The symmetry and stability of unstructured mesh C-grid shallow water models under the influence of coriolis. *Ocean Modelling* 2007; **16**:47–60.
7. Toro EF. *Shock-capturing Methods for Free-surface Shallow Flows*. Wiley: New York, 2001.
8. Alcrudo F, Garcia-Navarro P. A high-resolution Godunov-type scheme in finite volumes for the 2d shallow water equations. *International Journal for Numerical Methods in Fluids* 1993; **16**:489–505.
9. Perot B. Conservation properties of unstructured staggered mesh schemes. *Journal of Computational Physics* 2000; **159**:58–89.
10. Wenneker I, Segal A, Wesseling P. A mach-uniform unstructured staggered grid method. *International Journal for Numerical Methods in Fluids* 2002; **40**:1209–1235.
11. Casulli V, Walters RA. An unstructured grid, three-dimensional model based on the shallow water equations. *International Journal for Numerical Methods in Fluids* 2000; **32**:331–348.

DOI: 10.1002/fld

12. Bern MW, Eppstein D. Mesh generation and optimal triangulation. In *Computing in Euclidean Geometry* (2nd edn), Du D-Z, Hwang FK-M (eds). Lecture Notes Series on Computing, vol. 4. World Scientific: Singapore, 1995; 47–123.
13. Nujić M. Efficient implementation of non-oscillatory schemes for the computation of free-surface flows. *Journal of Hydraulic Research* 1995; **33**:101–111.
14. Lax P, Wendroff B. System of conservation laws. *Communications on Pure and Applied Mathematics* 1960; **13**:217–237.
15. Carlson BG. Solution of the transport equation by S_n approximations. *Technical Report LA-1891*, Los Alamos Scientific Laboratory, 1955.
16. Keller HB, Wendroff B. On the formulation and analysis of numerical methods for the time dependent transport equations. *Communications on Pure and Applied Mathematics* 1957; **10**:567–582.
17. Richtmyer RD, Morton KW. *Difference Methods for Initial Value Problems*. Interscience: New York, 1967.
18. Collins JP, Colella P, Glaz HM. An implicit–explicit Eulerian Godunov scheme for compressible flow. *Journal of Computational Physics* 1995; **116**:195–211.
19. O'Rourke PJ, Sahota MS. A variable explicit/implicit numerical method for calculating advection on unstructured meshes. *Journal of Computational Physics* 1998; **143**:312–345.
20. Shewchuk JR. Delaunay refinement algorithms for triangular mesh generation. *Computational Geometry* 2002; **22**:21–74.
21. Baker BS, Grosse E, Rafferty CS. Nonobtuse triangulation of polygons. *Discrete and Computational Geometry* 1988; **3**:147–168.
22. Bern M, Mitchell S, Ruppert J. Linear-size nonobtuse triangulation of polygons. *SCG '94*: *Proceedings of the Tenth Annual Symposium on Computational Geometry*, New York, NY, U.S.A. ACM: New York, 1994; 221–230.
23. Gerver JL. The dissection of a polygon into nearly equilateral triangles. *Geometriae Dedicata* (*Historical Archive*) 1984; **16**:93–106.
24. Maehara H. Acute triangulations of polygons. *European Journal of Combinatorics* 2002; **23**:45–55.
25. Ingram DM, Causon DM, Mingham CG. Developments in Cartesian cut cell methods. *Mathematics and Computers in Simulation* 2003; **61**:561–572.
26. Causon DM, Ingram DM, Mingham CG, Yang G, Pearson RV. Calculation of shallow water flows using a Cartesian cut cell approach. *Advances in Water Resources* 2000; **23**:545–562.
27. Rosatti G, Cesari D, Bonaventura L. Semi-implicit, semi-Lagrangian modelling for environmental problems on staggered cartesian grids with cut cells. *Journal of Computational Physics* 2005; **204**:353–377.
28. Wang J-W, Liu R-X. A comparative study of finite volume methods on unstructured meshes for simulation of 2d shallow water wave problems. *Mathematics and Computers in Simulation* 2000; **53**:171–184.
29. Hager WH, Schwalt M, Jimenez O, Chaudry MH. Supercritical flow near an abrupt wall deflection. *Journal of Hydraulic Research* 1994; **32**:103–118.
30. de Vriend HJ. Mathematical-model of steady flow in curved shallow channels. *Journal of Hydraulic Research* 1977; **15**:37–54.

DOI: 10.1002/fld